

pubs.acs.org/JPCC Article

New Means to Control Molecular Assembly

Jiali Zhang, Hai Yu, Bradley Harris, Yunbo Zheng, Umit Celik, Lan Na, Roland Faller, Xi Chen, Dominik R. Haudenschild, and Gang-yu Liu*



Cite This: J. Phys. Chem. C 2020, 124, 6405-6412



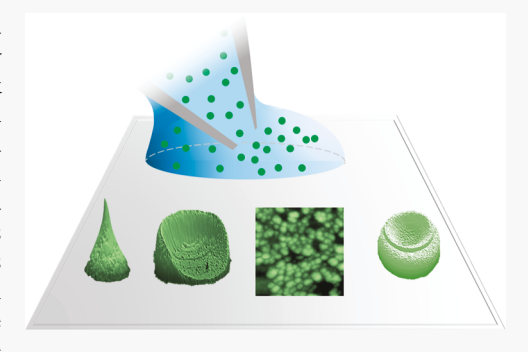
ACCESS

Metrics & More



SI Supporting Information

ABSTRACT: While self-assembly of molecules is relatively well-known and frequently utilized in chemical synthesis and materials science, controlled assembly of molecules represents a new concept and approach. The present work demonstrates the concept of controlled molecular assembly using a nonspherical biomolecule, heparosan tetrasaccharide (MW = 1.099 kD). The key to controlled assembly is the fact that ultrasmall solution droplets exhibit different evaporation dynamics from those of larger ones. Using an independently controlled microfluidic probe in an atomic force microscope, sub-femtoliter aqueous droplets containing designed molecules produce well-defined features with dimensions as small as tens of nanometers. The initial shape of the droplet and the concentration of solute within the droplet dictate the final assembly of molecules because of the ultrafast evaporation rate and dynamic spatial confinement of the droplets. The



level of control demonstrated in this work brings us closer to programmable synthesis for chemistry and materials science which can be used to develop vehicles for drug delivery and three-dimensional nanoprinting in additive manufacturing.

■ INTRODUCTION

Assembly of molecules into mesoscale structures by design still poses great challenges, despite pronounced advances in bottom-up and top-down approaches. 1,2 Self-assembly (SA) provides a powerful means to address this challenge. Ordered structures driven by thermodynamics have been reported, including self-assembled monolayers (SAMs),^{3–5} phase-separated polymers,^{6–9} and lipid bilayers.^{10,11} In attempts to produce molecular assemblies by design, the concept of controlled assembly was demonstrated in our previous study via the formation of various assemblies of spherical macromolecules, such as star polymers (MW = 383 kD, Rh = 47 nm). 12 The key to controlled molecular assembly relies on an ultrafast evaporation rate and spatial confinement by small droplets (sub-fL), as shown in Figure 1. The rapid evaporation locks the solute molecules in place, leading to a high degree of control over the feature geometry and intrafeature molecular packing. 12 The dynamic confinement was controlled by the regulation of volume and evaporation scenario such as constant contact area evaporation on solution-philic/hydrophilic surface ^{12–15} or constant contact angle evaporation on solution-phobic/hydrophobic surface. ^{12,13,16–20}

The present work pushes the concept of controlled assembly to smaller and nonspherical molecules, for example, heparosan tetrasaccharide (referred to as heparosan, MW = 1.099 kD), as shown in Figure 1. Heparosan is a polysaccharide consisting of disaccharide repeating units of α 1–4-linked *N*-acetyl-D-glucosamine (GlcNAc) and β 1–4-linked D-glucuronic acid (GlcA). It is produced as a capsule polysaccharide by both *Pasteurella multocida* Type D and *Escherichia coli* K5. It is also the

polysaccharide backbone of heparin and heparan sulfate found in mammals.²³ Assemblies of heparosan, for example, nanogels,²⁴ micelles,^{25–28} and nanoparticles,²⁹ have been used for disease diagnosis and treatment. The formation of these molecular assemblies relies primarily on SA.²⁴⁻²⁹ The size of such self-assembled units are typically in the range of 50-220 nm. 24-29 It was reported that the particle size, size distribution, and morphology play important roles in their efficacy, as these factors impact cell-uptake and blood circulation time, as well as drug release. 30 Using various predesigned ultrasmall droplets at defined solute concentration and initial droplet volume and geometry, this work demonstrates the feasibility for controlling molecular assembly of heparosan oligosaccharides. Specifically, the ability to control the assembly of heparosan nanostructures by design could significantly advance biomaterial development for drug delivery and theragnostic applications. In general, this level of control demonstrated in this work brings us closer to programmable synthesis for chemistry as well as developing vehicles for drug delivery and three-dimensional (3D) nanoprinting in additive manufacturing.

Received: December 8, 2019 Revised: February 16, 2020 Published: February 24, 2020



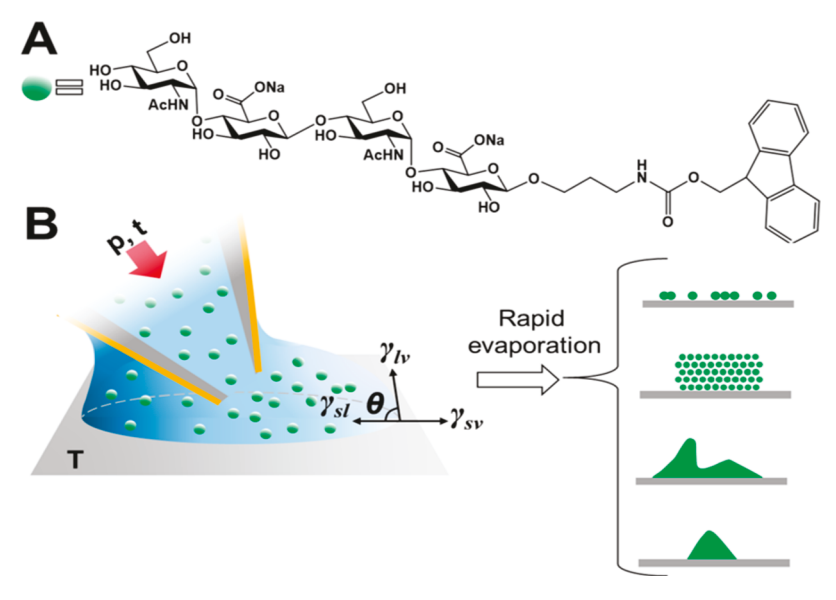


Figure 1. (A) Chemical structure of Fmoc-tagged heparosan tetrasaccharide. (B) Schematic diagram illustrating our concept of controlled assembly. An ultrasmall liquid droplet is delivered via a microfluidic probe to a surface with designed solvent-philicity. The droplet size and shape are dictated by the delivery parameters (e.g., p, t, T, and probe location), and droplet—surface interactions (θ and γ representing contact angle, and surface tensions at phase boundaries). The right column illustrates solute assemblies upon rapid solvent evaporation.

EXPERIMENTAL METHODS

Materials. Glass slides with lateral dimensions of 75 mm × 25 mm and thicknesses of 1 mm were purchased from Fisher Scientific (Pittsburgh, PA). Glycerol (≥99%), sulfuric acid (95.0-98.0%), hydrogen peroxide (30% aqueous solution), ammonium hydroxide (NH₄OH, 30% aqueous solution), and toluene (99.8%) were purchased from Sigma-Aldrich (St. Louis, MO). N-(6-Aminohexyl)-aminopropyltrimethoxysilane (AAPTMS) and octadecyltrichlorosilane (OTS) were purchased from Gelest (Morrisville, PA). Ethanol (99.5%) was purchased from KPTEC (King of Prussia, PA). Ultrapure water was attained from a Milli-Q water system with a resistance of 18.2 M Ω cm at 25 °C (EMD Millipore, Billerica, MA). Nitrogen gas (99.999%) was purchased from Praxair, Inc. (Danbury, CT, King of Prussia, PA). AC240TS-R3 silicon cantilevers were purchased from Oxford Instruments Asylum Research (Santa Barbara, CA). All other materials were used without further treatment or modification, unless otherwise stated.

Fluorenylmethoxycarbonyl (Fmoc)-tagged heparosan tetrasaccharide (referred to as "heparosan" hereafter) was chemoenzymatically synthesized from chemically synthesized Fmoctagged monosaccharide GlcA β ProNHFmoc using a sequential one-pot multienzyme (OPME) process with alternating OPME GlcNAc-activation/transfer and OPME GlcA-activation/transfer systems.³¹ Briefly, disaccharide GlcNAcα1-4GlcAβProNHFmoc was enzymatically synthesized from GlcAβProNHFmoc via a one-pot four-enzyme GlcNAcactivation and a transfer system containing Bifidobacterium longum N-acetylhexosamine-1-kinase (BLNahK),32 P. multocida N-acetylglucosamine-1-phosphate uridylyltransferase (PmGlmU), 33 P. multocida inorganic pyrophosphatase (PmPpA), 34 and Δ 80PmHS2. 31 Trisaccharide GlcA β 1-4GlcNAc α 1-4GlcA β ProNHFmoc was then synthesized from the disaccharide using a one-pot four-enzyme GlcA-activation and transfer system containing Arabidopsis thaliana glucuronokinase (AtGlcAK),³⁵ B. longum UDP-sugar pyrophosphorylase,³⁶ PmPpA, and Δ80PmHS2. Finally, the heparosan

tetrasaccharide was readily synthesized from the trisaccharide using the OPME GlcNAc-activation/transfer system containing BLNahK, PmGlmU, PmPpA, and $\Delta 80 PmHS2.^{31}$

Preparation of Self-Assembled Monolayers. The goal of this step is to prepare a set of surfaces with designated solution-philicity using SAMs on glass surfaces. Glass slides were cleaned following the previously reported protocols.^{37–43} In brief, substrates were cleaned using piranha solution by immersion for 1 h, then rinsed with copious quantities of ultrapure water. Piranha solution is a mixture of sulfuric acid and hydrogen peroxide at a (v/v) ratio of 3:1. It is highly corrosive and should be handled carefully. Then, the cleaned glass substrates were immersed in a prepared basic bath at 70 °C for 1 h. Basic bath is prepared by mixing ammonium hydroxide, hydrogen peroxide, and water at a (v/v) ratio of 5:1:1. Finally, substrates were rinsed again with copious quantities of ultrapure water and dried in nitrogen gas. The hydrophilicity of glass substrates was modified using silane chemistry, following established protocols.^{37–43} To modify glass slides with amine-terminated silane AAPTMS SAMs, the clean glass slides were placed into a sealed Teflon container (100 mL) containing 200 μ L of AAPTMS, then heated in an oven at 70-80 °C for 2 h. The substrate was then rinsed with ethanol and deionized water, sequentially, followed by drying in nitrogen gas. To prepare OTS-modified glass slides, freshly cleaned glass slides were immersed in a solution of 5 mM OTS in toluene for 30 min, followed by rinsing with toluene and ethanol, and then dried in nitrogen gas.

Contact Angle Measurement. Contact angle data were collected for the modified substrates with a VCA Optima Contact Angle Measurement system (AST Products, Billerica, MA), following standard protocols. $^{12,44-46}$ A 3 μ L drop of designated solution was placed on surfaces using an Hamilton 700 series HPLC needle (Hamilton Co., Reno, Nev.). At least three different positions per sample were tested to assure reproducibility and accuracy. For solution of heparosan with concentration of 2×10^{-5} M in a mixed solvent of glycerol/ $H_2O = 5.95$ (v/v), the contact angle on AAPTMS SAM and

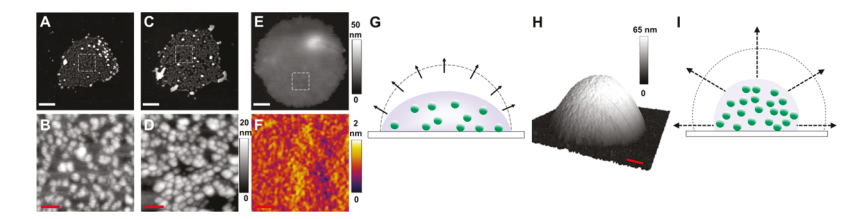


Figure 2. (A) AFM topographic image of a disk of heparosan formed after delivering a droplet under 20 mbar for 4.02 s on AAPTMS/glass. Solution concentration: 2×10^{-6} M. (B) Zoomed-in view of the defined area (square frame) in (A). (C) Similar to (A) except with high pressure and longer delivery time, 100 mbar and 5 s, respectively. (D) Zoom-in image as defined in (C). (E) Similar to (B) except higher concentration of heparosan, 2×10^{-5} M. (F) Zoom-in image of as-defined in (E) (squared area). (G) Schematic diagram illustrates the constant contact area evaporation of a droplet on a hydrophilic AAPTMS/glass surface. Broken line and array arrows represent initial droplet boundary, and evaporation direction and rate, respectively. (H) AFM topography of a mound formed on OTS/glass under the same delivery condition as (E). (I) Schematic diagram illustrates the constant contact angle evaporation for a droplet on a hydrophobic surface. The scale bars for white and red bars are 1 μ m and 200 nm, respectively.

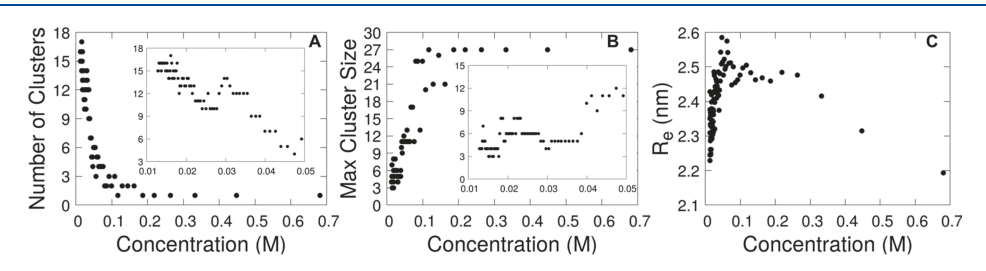


Figure 3. (A) Number of heparosan clusters during each simulation. Inlay is below 0.045 M (B) maximum number of heparosan in a cluster at any given state during simulations during evaporation. Inlay is below 0.045 M. (C) The average end-to-end distance of the heparosan during each simulation.

OTS SAM was 59° and 107° , respectively. Reducing the concentration to 2×10^{-6} M led to 63° on AAPTMS SAM and 102° on OTS SAM. For 2×10^{-5} M aqueous solutions, the contact angle was measured to be 67° on AAPTMS SAM and 104° on OTS SAM, which are very similar to the contact angle of pure water on AAPTMS $(58^{\circ})^{47,48}$ and OTS SAMs (110°) , 49,50 respectively.

Microfluidic Delivery of Ultrasmall Liquid Droplets. A state-of-the-art microfluidic system, FluidFM Bot, 12,51-54 equipped with an independent hollow probe was used to dispense heparosan solution down to attoliter volume onto the designated surfaces. This system combines an atomic force microscopy (AFM) probe assembly, a precise x-y motorized stage, an inverted optical microscope, and a pressure controller. The cantilever contains a microchannel and a reservoir and is connected to a pressure controller (-800 to 1000 mbar, 1 mbar precision) to dispense liquid inside the AFM head to guide the cantilever vertical movement. For optical view, an inverted microscope was used for imaging and facilitating stage control. A digital microscope was installed to monitor the laser position and probe movement. Microchanneled hollow probes with 300 nm square aperture at apex of the tip were utilized. The hollow probe was prefilled with designed heparosan tetrasaccharide solution, with a square pyramidal tip tilting 11° from the surface normal. The cantilevers were made of Si. Initially, 1 μ L of the designated heparosan tetrasaccharide solution was filled into the probe's 2 μ L reservoir. The contact force or load was set to 80 nN for all deliveries reported in this work.

AFM Characterization of Heparosan Assemblies. After droplet deposition, liquid evaporates rapidly as monitored via bright field optical microscopy. To avoid any residual solvent and facilitate AFM characterization, the glass slides were placed in a clean ambient environment overnight unless

specified. The AFM (MFP-3D, Oxford Instrument, Santa Barbara, CA) has a deflection configuration. Silicon probes (AC 240TS-R3, Olympus America, Central Valley, PA) have a force constant of 1.7 N/m and resonance frequency of 70 kHz. Tapping mode was utilized for imaging with damping set at 40–60%. The AFM images were analyzed using Asylum MFP-3D software developed on an Igor Pro 6.12 platform.

■ RESULTS AND DISCUSSION

Controlling Molecular Packing. Our previous work on the controlled assembly of star polymers demonstrated the packing can be controlled from random distribution to the closely packed structure within monolayer, bilayer, or multilayer disks. 12 The disk geometry is primarily attributed to constant area evaporation of the droplets on solution-philic surfaces. 12-15 In contrast to star polymers which are almost rigid with spherical shape, 12,55 individual heparosan molecules dissolved in aqueous solutions are flexible and linear, making them "semi-flexible rods". The critical question is whether our approach enables control over the packing of heparosan. Figure 2A shows a heparosan disk formed upon delivery and evaporation of a 2.56 pL droplet of 2×10^{-6} M heparosan tetrasaccharide solution onto a clean aminopropyltrimethoxysilane (AAPTMS) SAM surface. The AAPTMS SAM surface is solution-philic with a contact angle of 63°. Thus, the droplet appeared to spread. Upon evaporation, a disk was formed covering an 8.3 μ m² area, that is, the interfacial area of the initial droplet on the AAPTSM SAM surface. Within the disk, randomly distributed molecular clusters were clearly visible (bright features), as shown in Figure 2B. These clusters are relatively homogeneous in size and 3.5-9.5 nm in height. These clusters are well-separated, 40-220 nm among the nearest neighbors (NN). Increasing amount of materials delivered, for example, 4.36 pL droplets, led to larger disks, for example, a 11.2 μ m² area disk, as shown in Figure 2C. Within the disk, clusters of similar size to the clusters shown in Figure 2B are also seen, as shown in Figure 2D. These clusters exhibit heights of 12-18 nm with NN separation 18-39 nm, that is, similar in size but more closely packed than shown in Figure 2A. The formation of a disk containing randomly distributed solute clusters is consistent with constant contact area evaporation. 12-15 The presence of clusters instead of individual heparosan molecules is attributed to molecular clustering during evaporation, based on our molecular dynamics (MD) simulation (see below). Increasing heparosan tetrasaccharide concentration and/or amount further decreases the cluster separation. At 2×10^{-5} M and 0.833 pL, a heparosan disk was formed: 23.7 nm tall and 5.414 μ m wide, as shown in Figure 2E. Within the disk, clusters of heparosan are packed in an overcrowding way, as shown Figure 2F, manifesting to a smoother disk surface than lower coverage

The MD simulations (see details in Table S1) reveal a more detailed molecular process during evaporation. Indeed, the outcomes show a progression of heparosan from individual molecules in aqueous solution to aggregate, and then finally to a polymer melt. This is best seen quantitatively in Figure 3, suggesting the solution phase is below 0.04 M, a transition phase between 0.04 and 0.1 M, and a transition toward a polymer melt beginning at 0.3 M. While the actual concentration used in experiments is μM , the simulated concentrations were much higher than those used experimentally in order to speed up the aggregation trends to reasonable simulation times and to replicate the conditions of water removal leading to sugar molecules packing together. For the y axis in Figure 3, a cluster is 1 or more sugar molecules within an angstrom of another sugar molecule. For Figure 3A, this means that individual sugars appear on the y-axis as a cluster, that is, the maximum possible number of clusters is 27. Figure 3A,B taken together provides insight into the relevant range of concentrations for which aggregation begins. Insets in these figures are included to differentiate the concentrations and transition below 0.045 M. An understanding of what the sugars are doing in these regions is best seen by the end-to-end distance shown in Figure 3C. At concentrations below 0.04 M, the sugars have favorable enough interactions with water that they remain flexible and independent in solution. As the sugars are pushed together as concentration increases, the individual sugar molecules extend to find each other in solution and increase favorable interactions. This mechanism explains the presence of distributed aggregates or "clusters" observed in the experimental disk features. The concentration range for this transition corresponds to approximately 0.04-0.1 M. The maximum end-to-end distance in this region approximates the end-to-end distance obtained through ChemDraw (2.55 nm). This concentration range corresponding to chain expansion correlates to a decrease in the overall number of clusters and an increase in maximum cluster size, as shown in Figure 3A,B. Figure 4A-C provides a more direct visualization of the transition from individual molecules to a cluster in the MD simulations, as this can be a useful insight into the locations where aggregation sites occur. Additional simulation analysis for this transition behavior is presented in Figures S1 and S2 of the Supporting Information.

In our attempt to further increase molecular packing and form a mound geometry, constant contact angle evaporation was adopted. $^{12,13,16-20}$ In this case, droplets of heparosan

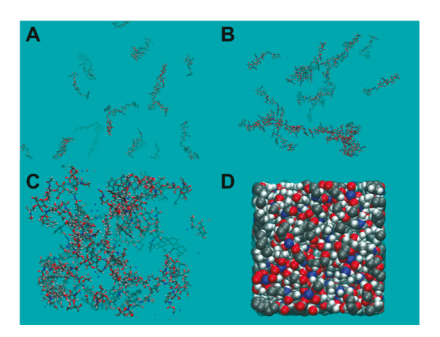


Figure 4. Ball-and-stick model displaying the molecular states from our MD simulation at (A) 0.0138 M, in a $15 \times 15 \times 15$ nm³ box; (B) 0.049 M in a $9.4 \times 9.4 \times 9.4$ nm³ box; and (C) 0.218 M in a $4.0 \times 4.0 \times 4.0$ nm³ box. (D) Volume-filling model from our MD simulation at 1.3 M in a $3.2 \times 3.2 \times 3.2$ nm³ box.

tetrasaccharide solution were delivered onto OTS SAM surfaces. The contact angle of the heparosan solution measured 107° , thus the droplets maintained a spherical hat geometry throughout evaporation. Evaporation of 0.113 pL of 2×10^{-5} M heparosan solution led to the mound formation, as shown in Figure 2H. The mound is 1.779 μ m wide at the base and 111.7 nm tall. The exterior of the mound appeared homogenous, as revealed in Figure 2H. In other words, the clusters collapsed and merged to form a single assembly. Given the spatial confinement and rapid evaporation, heparosan molecules were closely jammed within each assembly, analogous to the interdigitated state of chains among star polymers in a mound. This approach enables control over the size of each mound (or number of molecules in a single assembly), by varying the heparosan concentration and droplet volume.

Our MD simulations rationalize the transition from aggregates to this polymer-melt-like state. At concentrations above 0.3 M, corresponding to the final 4% of water molecules, a transition to the melt-like state is observed. The removal of the final few percent of water corresponds to a melt-like transition shown in Figure 3C. The end-to-end distance drops from the elongated molecules observed in the transitional and aggregate state. Under spatial confined situation, such as the constant-contact-angle evaporation, the molecules begin to follow a random walk as all interactions become equal among the other heparosan, compared to the self-avoiding walk the heparosan molecules experienced with competing interactions between the heparosan and water. Figure 4D shows a visualization of this state in the simulation.

Control over the Geometry of Individual Features. As discussed in the introduction, the ultrasmall droplet size and rapid evaporation are keys to achieving controlled molecular assembly. While previous sections addressed the molecular packing within each feature upon initial delivery of spherical hat-shaped droplets, this section reports nonspherical hat-shaped droplets, leading to assemblies of solutes in more complex geometries than simple disks or mounds.

Figure 5A shows 4×4 arrays of "volcano-like" features. Each feature was produced by dispensing 154 fL of 2×10^{-5} M heparosan tetrasaccharide solution onto an AAPTMS SAM covered glass surface. The delivery conditions: t = 1 s, p = 100 mbar with a contact force of 80 nN. Individual features can be clearly visualized, as shown in Figure 5B: base diameter of $1.95-2.33~\mu m$ and with the volcanic height of 23.9-31.5 nm. The top opening measures $0.95-1.25~\mu m$ wide and 5.6-11 nm deep. The formation of this geometry is illustrated in Figure

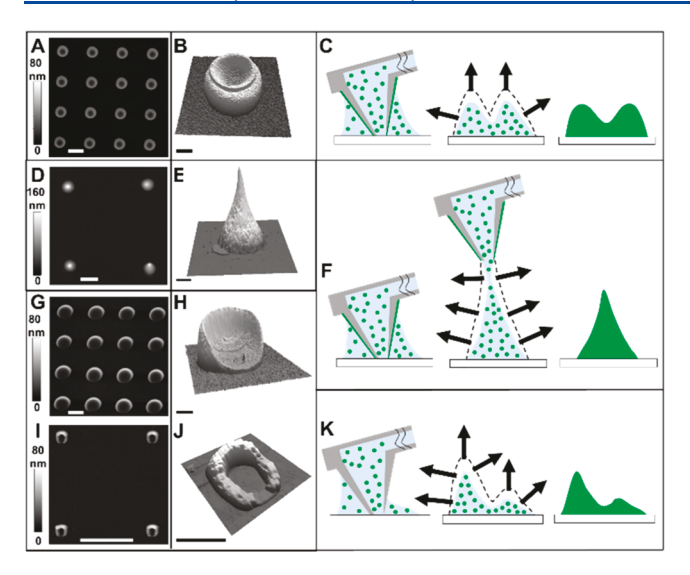


Figure 5. (A) AFM topographic image of a 4 × 4 array of heparosan assemblies exhibiting volcano-like shape. (B) 3D display of a single feature from (A) revealing clearly the volcano-shaped geometry. (C) Schematic diagram illustrating characteristic moment of controlled assembly: during dispensing, immediately after probe withdrawal, and final assembly after solvent evaporation. Constant contact area evaporation occurred. The broken line and array arrows represent initial droplet boundary, and evaporation direction and rate, respectively. (D) AFM topographic image of a 2 × 2 array of heparosan assemblies with teepee-like shape. (E) 3D display of a single feature from (D) revealing clearly the teepee geometry. (F) Schematic diagram illustrating the assembly leading to teepee shape geometry. (G) AFM topographic image of a 4 × 4 array of heparosan assemblies exhibiting asymmetry. (H) 3D display of a single feature from (G) clearly revealing the bean-bag geometry. (K) Schematic diagram illustrates the assembly leading to asymmetric geometry. (I) AFM topographic image of a 2 × 2 array of heparosan assemblies exhibiting asymmetry. (J) 3D display of a single feature from (I). Scale bars are 2500 and 500 nm for white and black bars, separately. Z-scale in the 3D displays is exaggerated to allow clear visualization of the feature geometry.

5C. The exterior of the tip apex was pretreated by dipping it into the solution and then letting it dry. Thus, the exterior of the tip apex becomes very solution-philic, leading to symmetric climbing of liquid during delivery via capillary interactions. The evaporation is faster than that shown in Figure 2 because the solvent here is pure water. Therefore, the final assembly adopts a similar geometry to the initial droplet. The upper "lip" was likely formed during the final separation of the tip from the droplet, when the residual amount of liquid fell atop of the partially evaporated droplet. The result shown in Figure 5A is reproducible and robust, as taller volcanos were produced by increasing the amount of material delivered, for example, taller volcanos than the one shown in Figure 5A were produced (height = 42.4-87.1 nm) by increasing injection time from 1 to 3 s under delivery pressure of 400 mbar (more detailed outputs are included in Figure S3 and Table S2 in the Supporting Information).

The proposed mechanism is further validated by forming "teepee" features, a 2 \times 2 array shown in Figure 5D, under identical conditions except using a mixed solvent of glycerol/ $H_2O=5:95~(v/v)$ and lower concentration of 2 \times 10⁻⁶ M. Adding the small amount (5%) of glycerol slowed down the evaporation, allowing the solvent to merge and form capillary neck upon retreat of the tip, as illustrated in Figure 5F. The

sharp tent top, clearly visible in Figure 5E, is due to the capillary neck formed at the final withdrawal. Further addition of glycerol could increase stickiness and viscosity of the solution, leading to the sharper and longer tent top, as illustrated in Figure 5F. The features shown in Figure 5D have a base diameter of 2.07–2.29 μ m, and a height of 140–180 nm. The results were reproducible and robust. Under the same dwelling time of 0.5 s, increasing injection pressure from 500 to 900 mbar leads to increased teepee base (from 1.20 to 2.02 μ m) and height (from 54 to 165 nm).

Without pretreatment of the tip, asymmetric features, such as "bean-bag," were formed, as shown in Figure 5G (a 4 × 4 array). The concentration of heparosan was 2×10^{-5} M in pure water. At dwelling time of 1 s and injection pressure of 100 mbar, 176 fL of solution was delivered onto a clean and hydrophilic AAPTMS glass. As clearly shown in Figure 5H, the bean-bag measures 2.42-2.8 μm at base diameter, with high and low edges of 45.4-52.4 and 3.3-6.1 nm, respectively. We were able to tune the size of the beanbag by varying the amount of material delivered. The formation of these asymmetric geometries are illustrated in Figure 5K. In contrast to Figure 5C, the droplet did not exhibit significant climbing up the apex exterior surfaces, instead it adopts a geometry guided by the local contact angle, as shown in Figure 5K. Since the probe tilted 11° from the surface normal, the droplet adopted an asymmetric geometry. With the fast evaporation of water, the initial droplet shape dictated the final assembly of the solutes, leading to the bean-bag shaped features. Reducing the amount of material, further lowering the symmetry, as shown in Figure 5I, a 4 × 4 array of "horseshoe" features was formed. Each feature represents a heparosan assembly, after dispensing 78.4 aL of 0.01 M heparosan aqueous solution on to the surfaces and drying. The horseshoe geometry is clearly visible in Figure 5J, with the maximum height of 95.7 nm. The full width at half maximum for both sides measure 137-153 and 143-161 nm with a separation of 307-359 nm. These results, collectively, demonstrate the high degree of control over the geometry of the molecular assembly by controlling the initial droplet geometry. Being stored in a clean environment under ambient conditions, these heparosan structures are stable beyond 4 months, based on time-dependent AFM imaging.

Applying Controlled Molecular Assembly to Enable **3D Nanoprinting.** With the knowledge gained above, that is, control over the assembly of heparosan via controlling the droplets dispensed, 3D nanoprinting shall be achievable by continuous delivery of solutions following the designed trajectory. The key is maintaining consistent and homogenous assembly of heparosan throughput the printing process. In other words, the controlled molecular assembly must be maintained at each transient spot of printing. Figure 6A demonstrates that lines of heparosan can be printed. Heparosan solution $(2 \times 10^{-5} \text{ M})$ was delivered continuously on an AAPTMS/Si SAM surface under p = 100 mbar, at a speed of 10 μ m/s. Under the delivery conditions, the transient time at each point is equivalent to a droplet deposition with dwell time of 0.4 s. Therefore, after solvent evaporation, the heparosan assembled into continuous lines with a high degree of consistency and homogeneity. All 25 lines are 50 μ m long, 116 nm wide and 26 nm tall, 5 of which are as shown in Figure 6A. The separation among the lines shown in Figure 6A measures 2.15, 2.09, 2.18, and 1.87 μ m, respectively, from right to left. The reproducibility was demonstrated by repeating the

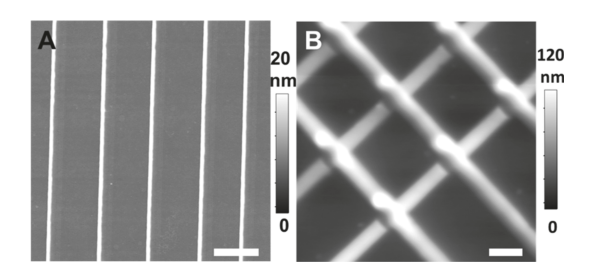


Figure 6. (A) 15 μ m × 15 μ m AFM topographic image of an array of heparosan lines. (B) 15 μ m × 15 μ m AFM topographic image of stacking grids consisting of heparosan. Scale bars are 2 μ m.

identical printing arrays of lines with the same geometry and size. The homogeneity and the size of the lines is consistent with the mechanism: at each point of delivery, constant area evaporation occur rapidly analogous to that shown in Figure 2G. The line width is tunable by the concentration and speed, for example, slower speed leads to wider lines.

Stacking grids, each layer perpendicular to another, were also printed under 200 mbar pressure, and at 2 μ m/s speed. The grids covered a 15 μ m × 15 μ m area, with a portion shown in the AFM image in Figure 6B. Each line 39–57 nm tall and 1.01–1.09 μ m wide, with periodicity or separation of 5 μ m. The height of the cross section was measured to be 55–69 nm tall. The angle between top and bottom line arrays are 90.0°. The high fidelity following the design demonstrates the feasibility for 3D nanoprinting using functional molecules such as heparosan.

CONCLUSIONS

Using heparosan tetrasaccharide as the functional solute, this work demonstrates our new concept of the controlled assembly of molecules. The key to the controlled assembly is the fact that ultrasmall solution droplets follow different evaporation dynamics from those of larger ones. The initial shape of the droplet and the concentration of the solute within the droplet dictate the evaporation mechanism and the final assembly of molecules due to the ultrafast evaporation rate and dynamic spatial confinement of the droplets. The level of control demonstrated in this work brings us closer to programmable synthesis and assembly for chemistry and materials science. Work is in progress to investigate temperature dependence of delivery, evaporation, and the assembly behavior. Future work also includes exploring its application in production of drug delivery vehicles and 3D nanoprinting in additive manufacturing.

ASSOCIATED CONTENT

Supporting Information

The Supporting Information is available free of charge at https://pubs.acs.org/doi/10.1021/acs.jpcc.9b11377.

MD simulation details and additional analysis; and experimental robustness; controlled assembly SI.doc. myffnonbonded.itp MDs forcefield for FMOC-heparosan tetrasaccharide using itp file type (PDF)

AUTHOR INFORMATION

Corresponding Author

Gang-yu Liu — Department of Chemistry, University of California Davis, Davis, California 95616, United States; orcid.org/0000-0003-3689-0685; Phone: (530) 754-9678; Email: gyliu@ucdavis.edu; Fax: (530) 754-8557

Authors

Jiali Zhang — Department of Chemistry, University of California Davis, Davis, California 95616, United States

Hai Yu — Department of Chemistry, University of California Davis, Davis, California 95616, United States; ⊚ orcid.org/ 0000-0002-4378-0532

Bradley Harris — Department of Chemical Engineering, University of California Davis, Davis, California 95616, United States

Yunbo Zheng — Department of Chemistry, University of California Davis, Davis, California 95616, United States

Umit Celik – Department of Chemistry, University of California Davis, Davis, California 95616, United States

Lan Na – Department of Chemistry, University of California Davis, Davis, California 95616, United States

Roland Faller — Department of Chemical Engineering, University of California Davis, Davis, California 95616, United States; Orcid.org/0000-0001-9946-3846

Xi Chen – Department of Chemistry, University of California Davis, Davis, California 95616, United States; orcid.org/0000-0002-3160-614X

Dominik R. Haudenschild – Department of Orthopaedic Surgery, University of California, Davis Medical Center, Sacramento, California 95817, United States

Complete contact information is available at: https://pubs.acs.org/10.1021/acs.jpcc.9b11377

Note:

The authors declare no competing financial interest.

ACKNOWLEDGMENTS

We thank Drs. Pablo Dörig and Dario Ossola from Cytosurge, Glattbrugg, Switzerland, for the helpful scientific discussions, and Susan Stagner for careful proof-reading. This work is supported by the Gordon and Betty Moore Foundation, the National Science Foundation (CHE-1808829), the Lawrence Livermore National Laboratory LDRD project 19-ERD-012 under the department of Energy Contract DE-AC52-07NA27344, UC Davis, and the National Institutes of Health (NIH) Common Fund Glycoscience Program grant, U01GM125288 and 1R01AR070239-01A1.

REFERENCES

- (1) Whitesides, G. M.; Grzybowski, B. Self-assembly at all scales. *Science* **2002**, 295, 2418–2421.
- (2) Xia, Y.; Whitesides, G. M. Soft lithography. *Annu. Rev. Mater. Sci.* **1998**, 28, 153–184.
- (3) Bain, C. D.; Troughton, E. B.; Tao, Y. T.; Evall, J.; Whitesides, G. M.; Nuzzo, R. G. Formation of monolayer films by the spontaneous assembly of organic thiols from solution onto gold. *J. Am. Chem. Soc.* **1989**, *111*, 321–335.
- (4) Sagiv, J. Organized monolayers by adsorption. 1. Formation and structure of oleophobic mixed monolayers on solid surfaces. *J. Am. Chem. Soc.* **1980**, *102*, 92–98.
- (5) Nuzzo, R. G.; Allara, D. L. Adsorption of bifunctional organic disulfides on gold surfaces. *J. Am. Chem. Soc.* **1983**, *105*, 4481–4483.
- (6) Hillmyer, M. A.; Bates, F. S.; Almdal, K.; Mortensen, K.; Ryan, A. J.; Fairclough, J. P. A. Complex phase behavior in solvent-free nonionic surfactants. *Science* **1996**, *271*, *976*–*978*.

- (7) Hayward, R. C.; Pochan, D. J. Tailored Assemblies of Block Copolymers in Solution: It Is All about the Process. *Macromolecules* **2010**, *43*, 3577–3584.
- (8) Pochan, D. J.; Chen, Z. Y.; Cui, H. G.; Hales, K.; Qi, K.; Wooley, K. L. Toroidal triblock copolymer assemblies. *Science* **2004**, *306*, 94–97.
- (9) Bigioni, T. P.; Lin, X.-M.; Nguyen, T. T.; Corwin, E. I.; Witten, T. A.; Jaeger, H. M. Kinetically driven self assembly of highly ordered nanoparticle monolayers. *Nat. Mater.* **2006**, *5*, 265–270.
- (10) Nagle, J. F.; Tristram-Nagle, S. Structure of lipid bilayers. *Biochim. Biophys. Acta, Rev. Biomembr.* **2000**, 1469, 159–195.
- (11) Groves, J. T.; Ulman, N.; Boxer, S. G. Micropatterning fluid lipid bilayers on solid supports. *Science* 1997, 275, 651–653.
- (12) Zhang, J.; Piunova, V. A.; Liu, Y.; Tek, A.; Yang, Q.; Frommer, J.; Liu, G.-y.; Sly, J. Controlled Molecular Assembly via Dynamic Confinement of Solvent. *J. Phys. Chem. Lett.* **2018**, *9*, 6232–6237.
- (13) Chhasatia, V. H.; Sun, Y. Interaction of bi-dispersed particles with contact line in an evaporating colloidal drop. *Soft Matter* **2011**, *7*, 10135–10143.
- (14) Ko, H.-Y.; Park, J.; Shin, H.; Moon, J. Rapid Self-Assembly of Monodisperse Colloidal Spheres in an Ink-Jet Printed Droplet. *Chem. Mater.* **2004**, *16*, 4212–4215.
- (15) Park, J.; Moon, J. Control of colloidal particle deposit patterns within picoliter droplets ejected by ink-jet printing. *Langmuir* **2006**, 22, 3506–3513.
- (16) Erbil, H. Y.; McHale, G.; Newton, M. I. Drop evaporation on solid surfaces: constant contact angle mode. *Langmuir* **2002**, *18*, 2636–2641.
- (17) Kuang, M.; Wang, J.; Bao, B.; Li, F.; Wang, L.; Jiang, L.; Song, Y. Inkjet Printing Patterned Photonic Crystal Domes for Wide Viewing-Angle Displays by Controlling the Sliding Three Phase Contact Line. *Adv. Opt. Mater.* **2014**, *2*, 34–38.
- (18) Kuncicky, D. M.; Velev, O. D. Surface-guided templating of particle assemblies inside drying sessile droplets. *Langmuir* **2008**, *24*, 1371–1380.
- (19) Picknett, R. G.; Bexon, R. The evaporation of sessile or pendant drops in still air. *J. Colloid Interface Sci.* **1977**, *61*, 336–350.
- (20) Zhong, X.; Crivoi, A.; Duan, F. Sessile nanofluid droplet drying. *Adv. Colloid Interface Sci.* **2015**, 217, 13–30.
- (21) Wang, Z.; Dordick, J. S.; Linhardt, R. J. Escherichia coli K5 heparosan fermentation and improvement by genetic engineering. *Bioeng. Bugs* **2011**, *2*, 63–67.
- (22) DeAngelis, P. L.; Gunay, N. S.; Toida, T.; Mao, W.-j.; Linhardt, R. J. Identification of the capsular polysaccharides of Type D and F Pasteurella multocida as unmodified heparin and chondroitin, respectively. *Carbohydr. Res.* **2002**, 337, 1547–1552.
- (23) Sismey-Ragatz, A. E.; Green, D. E.; Otto, N. J.; Rejzek, M.; Field, R. A.; DeAngelis, P. L. Chemoenzymatic synthesis with distinct Pasteurella heparosan synthases: monodisperse polymers and unnatural structures. *J. Biol. Chem.* **2007**, 282, 28321–28327.
- (24) Rippe, M.; Stefanello, T. F.; Kaplum, V.; Britta, E. A.; Garcia, F. P.; Poirot, R.; Companhoni, M. V. P.; Nakamura, C. V.; Szarpak-Jankowska, A.; Auzély-Velty, R. Heparosan as a potential alternative to hyaluronic acid for the design of biopolymer-based nanovectors for anticancer therapy. *Biomater. Sci.* 2019, 7, 2850–2860.
- (25) Chen, J.-X.; Zhang, M.; Liu, W.; Lu, G.-Z.; Chen, J.-H. Construction of serum resistant micelles based on heparosan for targeted cancer therapy. *Carbohydr. Polym.* **2014**, *110*, 135–141.
- (26) Qiu, L.; Shan, X.; Long, M.; Ahmed, K. S.; Zhao, L.; Mao, J.; Zhang, H.; Sun, C.; You, C.; Lv, G.; Chen, J. Elucidation of cellular uptake and intracellular trafficking of heparosan polysaccharide-based micelles in various cancer cells. *Int. J. Biol. Macromol.* **2019**, *130*, 755–764.
- (27) Sun, C.; Li, X.; Du, X.; Wang, T. Redox-responsive micelles for triggered drug delivery and effective laryngopharyngeal cancer therapy. *Int. J. Biol. Macromol.* **2018**, *112*, 65–73.
- (28) Qiu, L.; Ge, L.; Long, M.; Mao, J.; Ahmed, K. S.; Shan, X.; Zhang, H.; Qin, L.; Lv, G.; Chen, J. Redox-responsive biocompatible nanocarriers based on novel heparosan polysaccharides for intra-

- cellular anticancer drug delivery. Asian J. Pharm. Sci. 2018, DOI: 10.1016/j.ajps.2018.11.005.
- (29) Chen, J.-X.; Liu, W.; Zhang, M.; Chen, J.-H. Heparosan based negatively charged nanocarrier for rapid intracellular drug delivery. *Int. J. Pharm.* **2014**, 473, 493–500.
- (30) Danaei, M.; Dehghankhold, M.; Ataei, S.; Hasanzadeh Davarani, F.; Javanmard, R.; Dokhani, A.; Khorasani, S.; Mozafari, M. Impact of particle size and polydispersity index on the clinical applications of lipidic Nanocarrier Systems. *Pharmaceutics* **2018**, *10*, 57
- (31) Na, L.; Yu, H.; Ghosh, T.; McArthur, J. B.; Asbell, T.; Chen, X. Engineered *P. multocida* heparosan synthases improve size-controlled enzymatic synthesis of longer heparosan oligosaccharides. Submitted.
- (32) Li, Y.; Yu, H.; Chen, Y.; Lau, K.; Cai, L.; Cao, H.; Tiwari, V. K.; Qu, J.; Thon, V.; Wang, P. G.; Chen, X. Substrate promiscuity of Nacetylhexosamine 1-kinases. *Molecules* **2011**, *16*, 6396–6407.
- (33) Chen, Y.; Thon, V.; Li, Y.; Yu, H.; Ding, L.; Lau, K.; Qu, J.; Hie, L.; Chen, X. One-pot three-enzyme synthesis of UDP-GlcNAc derivatives. *Chem. Commun.* **2011**, *47*, 10815–10817.
- (34) Lau, K.; Thon, V.; Yu, H.; Ding, L.; Chen, Y.; Muthana, M. M.; Wong, D.; Huang, R.; Chen, X. Highly efficient chemoenzymatic synthesis of beta1-4-linked galactosides with promiscuous bacterial beta1-4-galactosyltransferases. *Chem. Commun.* **2010**, *46*, 6066–6068.
- (35) Muthana, M. M.; Qu, J.; Xue, M.; Klyuchnik, T.; Siu, A.; Li, Y.; Zhang, L.; Yu, H.; Li, L.; Wang, P. G.; Chen, X. Improved one-pot multienzyme (OPME) systems for synthesizing UDP-uronic acids and glucuronides. *Chem. Commun.* **2015**, *51*, 4595–4598.
- (36) Muthana, M. M.; Qu, J.; Li, Y.; Zhang, L.; Yu, H.; Ding, L.; Malekan, H.; Chen, X. Efficient one-pot multienzyme synthesis of UDP-sugars using a promiscuous UDP-sugar pyrophosphorylase from Bifidobacterium longum (BLUSP). *Chem. Commun.* **2012**, 48, 2728–2730.
- (37) Li, J.-R.; Lusker, K. L.; Yu, J.-J.; Garno, J. C. Engineering the spatial selectivity of surfaces at the nanoscale using particle lithography combined with vapor deposition of organosilanes. *ACS Nano* 2009, 3, 2023–2035.
- (38) Li, J.-R.; Garno, J. C. Elucidating the role of surface hydrolysis in preparing organosilane nanostructures via particle lithography. *Nano Lett.* **2008**, *8*, 1916–1922.
- (39) Lin, W.-f.; Swartz, L. A.; Li, J.-R.; Liu, Y.; Liu, G.-y. Particle Lithography Enables Fabrication of Multicomponent Nanostructures. *J. Phys. Chem. C* **2013**, *117*, 23279–23285.
- (40) Lin, W.-f.; Li, J.-R.; Liu, G.-y. Near-Field Scanning Optical Microscopy Enables Direct Observation of Moire Effects at the Nanometer Scale. *ACS Nano* **2012**, *6*, 9141–9149.
- (41) Garno, J. C.; Batteas, J. D. Nanofabrication with self-assembled monolayers by scanning probe lithography. In *Applied Scanning Probe Methods IV: Industrial Applications*; Springer Science & Business Media, 2006; pp 105–135.
- (42) Tian, T.; LeJeune, Z. M.; Serem, W. K.; Yu, J. J.; Garno, J. C. Nanografting: A method for bottom-up fabrication of designed nanostructures. In *Tip-Based Nanofabrication: Fundamentals and Applications*; Springer Science & Business Media, 2011; pp 167–205.
- (43) Lifang Shi, A. K.; Zhao, J.; Salmeron, M.; Liu, G. Y. High-Resolution Imaging of Cells Using Current Sensing Atomic Force Microscopy. *Lett. Appl. NanoBioScience* **2015**, *4*, 316–320.
- (44) Abbott, N. L.; Gorman, C. B.; Whitesides, G. M. Active control of wetting using applied electrical potentials and self-assembled monolayers. *Langmuir* **1995**, *11*, 16–18.
- (45) Bain, C. D.; Whitesides, G. M. A study by contact angle of the acid-base behavior of monolayers containing. omega.-mercaptocarboxylic acids adsorbed on gold: an example of reactive spreading. *Langmuir* 1989, 5, 1370–1378.
- (46) Yuan, W.; Van Ooij, W. J. Characterization of organofunctional silane films on zinc substrates. *J. Colloid Interface Sci.* **1997**, *185*, 197–209
- (47) Sugimura, H.; Hayashi, K.; Saito, N.; Nakagiri, N.; Takai, O. Surface potential microscopy for organized molecular systems. *Appl. Surf. Sci.* **2002**, *188*, 403–410.

- (48) Hayashi, K.; Saito, N.; Sugimura, H.; Takai, O.; Nakagiri, N. Surface potential contrasts between silicon surfaces covered and uncovered with an organosilane self-assembled monolayer. *Ultramicroscopy* **2002**, *91*, 151–156.
- (49) Mirji, S. A. Octadecyltrichlorosilane adsorption kinetics on Si (100)/SiO2 surface: contact angle, AFM, FTIR and XPS analysis. *Surf. Interface Anal.* **2006**, *38*, 158–165.
- (50) Wang, Y.; Lieberman, M. Growth of ultrasmooth octadecyltrichlorosilane self-assembled monolayers on SiO2. *Langmuir* **2003**, *19*, 1159–1167.
- (51) Ventrici de Souza, J.; Liu, Y.; Wang, S.; Dörig, P.; Kuhl, T. L.; Frommer, J.; Liu, G.-y. Three-dimensional nanoprinting via direct delivery. *J. Phys. Chem. B* **2017**, *122*, 956–962.
- (52) Deng, W. N.; Wang, S.; Ventrici de Souza, J.; Kuhl, T. L.; Liu, G.-y. New Algorithm to Enable Construction and Display of 3D Structures from Scanning Probe Microscopy Images Acquired Layer-by-Layer. *J. Phys. Chem. A* **2018**, 122, 5756–5763.
- (53) Meister, A.; Gabi, M.; Behr, P.; Studer, P.; Vörös, J.; Niedermann, P.; Bitterli, J.; Polesel-Maris, J.; Liley, M.; Heinzelmann, H.; Zambelli, T. FluidFM: combining atomic force microscopy and nanofluidics in a universal liquid delivery system for single cell applications and beyond. *Nano Lett.* **2009**, *9*, 2501–2507.
- (54) Grüter, R. R.; Vörös, J.; Zambelli, T. FluidFM as a lithography tool in liquid: spatially controlled deposition of fluorescent nanoparticles. *Nanoscale* **2013**, *5*, 1097–1104.
- (55) Lee, V. Y.; Havenstrite, K.; Tjio, M.; McNeil, M.; Blau, H. M.; Miller, R. D.; Sly, J. Nanogel Star Polymer Architectures: A Nanoparticle Platform for Modular Programmable Macromolecular Self-Assembly, Intercellular Transport, and Dual-Mode Cargo Delivery. Adv. Mater. 2011, 23, 4509—4515.